## Supplementary materials for TCD submission

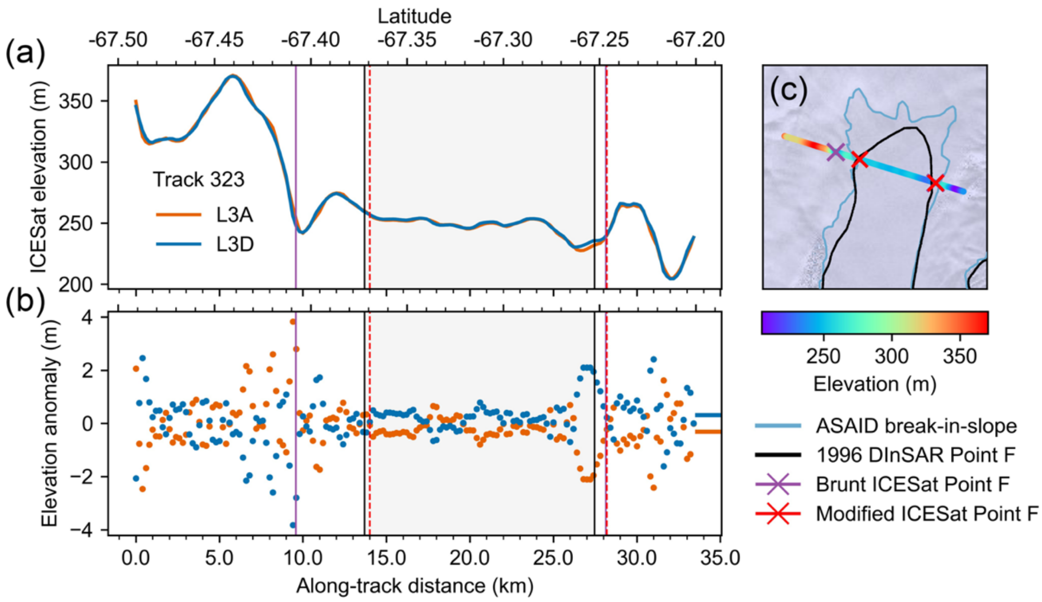


Figure S1. The ICESat-derived elevations (a) and elevation anomalies (b) along the RGT 323 at the main glacier trunk of the MUIS (c) processed in this study. The grey regions in (a) and (b) are the 1996 MEaSUREs DInSAR-derived ice shelf (Rignot et al., 2011, 2016). In subplots (a) and (b), the purple solid vertical lines are the Brunt et al. (2011) ICESat-derived Point F, the red dashed vertical lines are the manual-picked Point F based on elevation anomalies from repeat tracks L3A (June 21 – November 8, 2004) and L3D (June 23 – November 24, 2005). In (c), the data are overlaid on the Landsat Image Mosaic of Antarctica (Bindschadler et al., 2008).

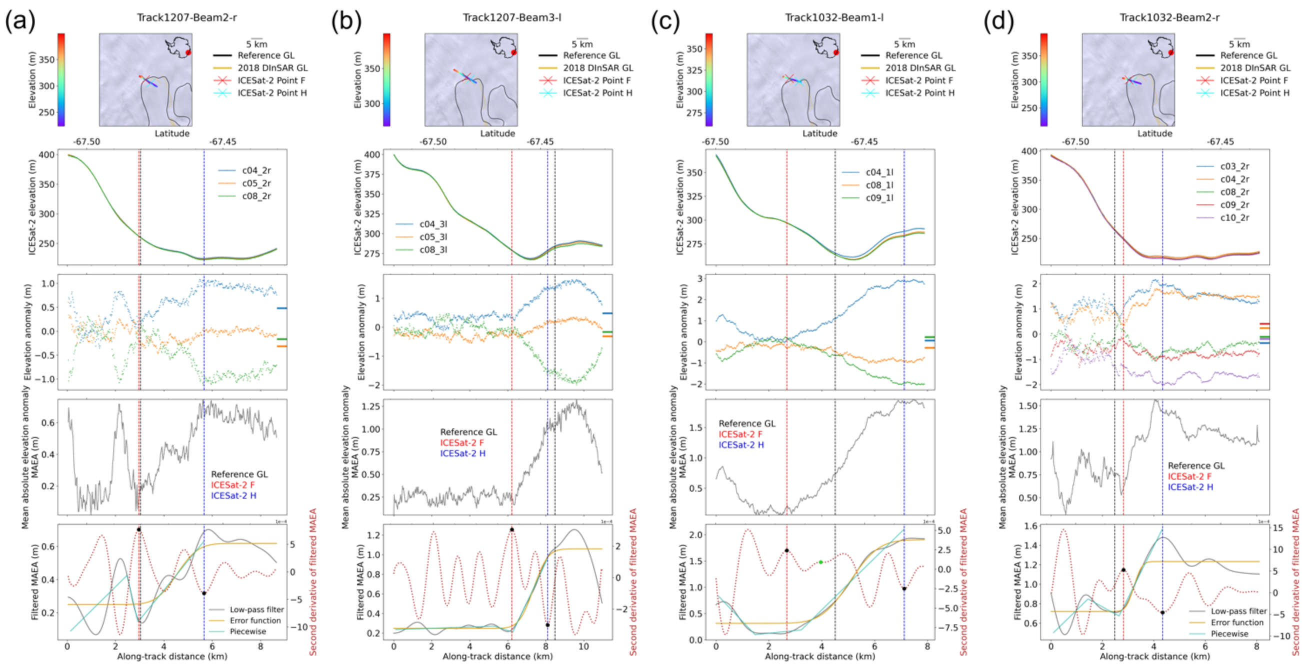


Figure S2. The repeat track analysis of ICESat-2 elevation profiles on the Totten Glacier Ice Shelf main glacier trunk along track 1207 GT2R (a), track 1207 GT3L (b), track 1032 GT1L (c) and track 1032 GT2R (d), respectively.

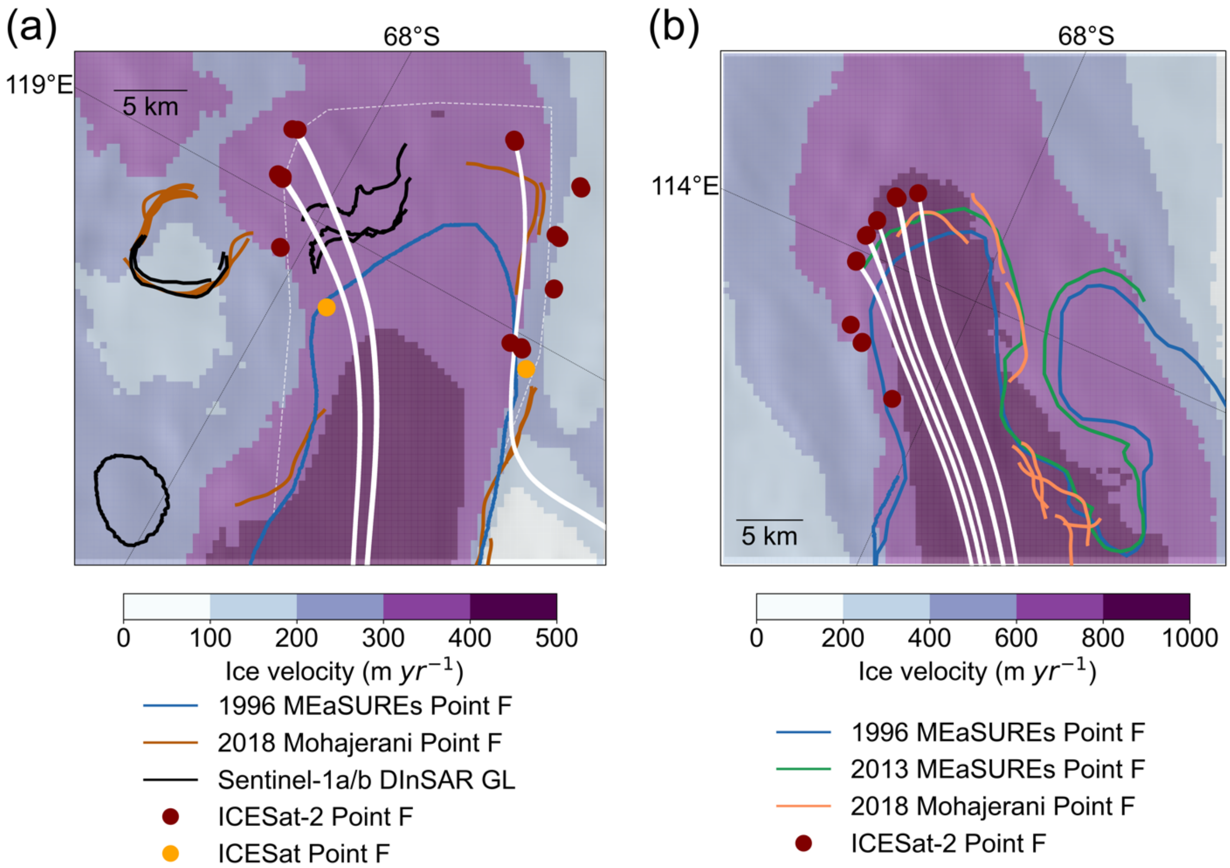


Figure S3. The ice flowlines used to measure the grounding line migrations between different time stamps at the main glacier trunks for Moscow University Ice Shelf (a) and the Totten Glacier Ice Shelf (b).

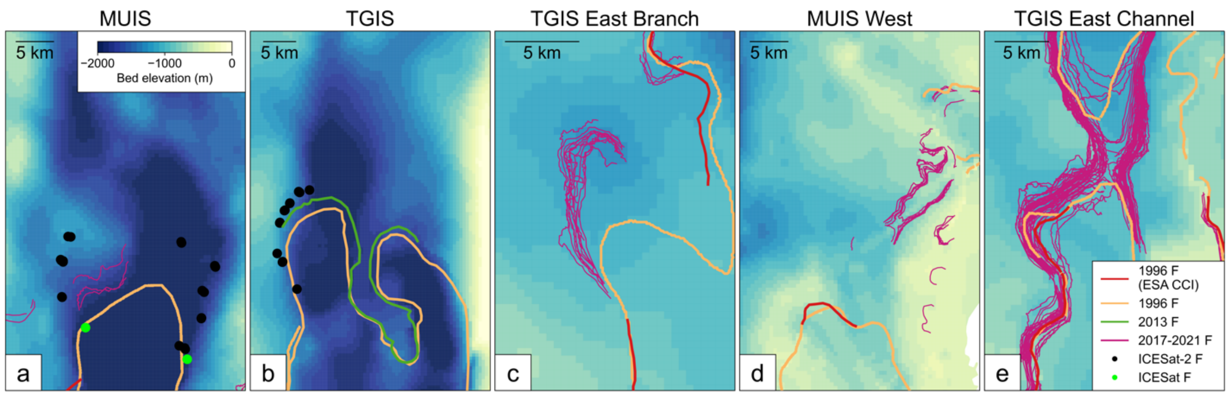


Figure S4. BedMachine bed elevation (Morlighem et al., 2020) overlaid with different grounding zone products. The ESA CCI DInSAR grounding line in 1996 is shown as the red solid line (ESA, 2017).

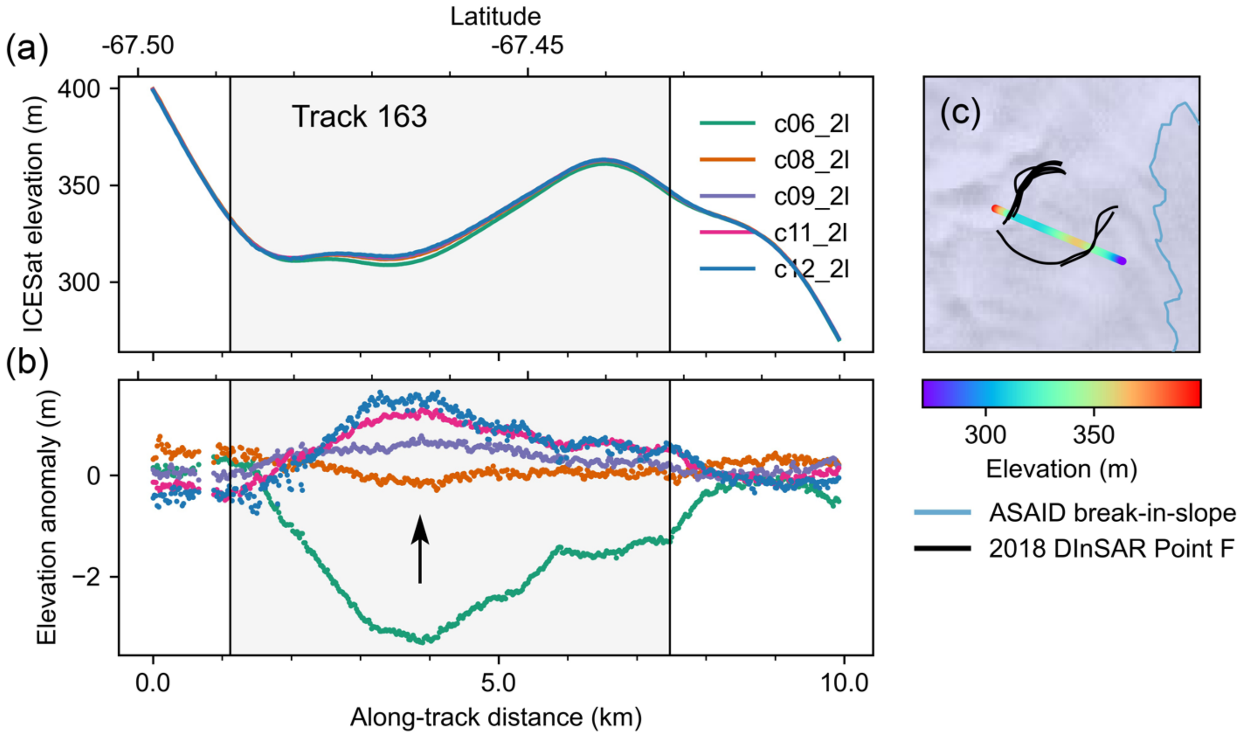


Figure S5. The ICESat-2-derived elevations (a) and elevation anomalies (b) along the track 163 GT2L across the MUIS southern subglacial lake (c). The grey regions in (a) and (b) are the subglacial lake boundary from 2018 Sentinel-1a/b DInSAR grounding line product (Mohajerani et al., 2021). In (c), the data are overlaid on the Landsat Image Mosaic of Antarctica (Bindschadler et al., 2008). The ICESat-2 data used in detecting subglacial lake is version 5 between 30 March 2019 and 22 December 2021.

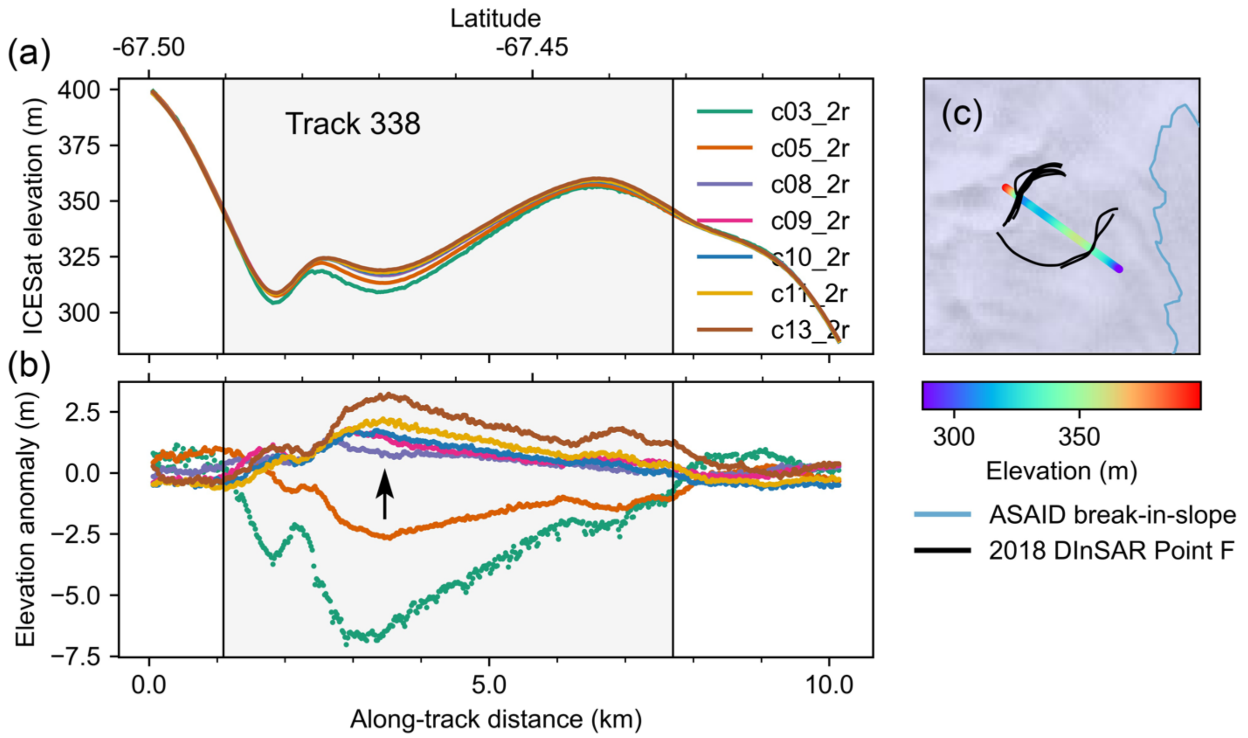


Figure S6. The ICESat-2-derived elevations (a) and elevation anomalies (b) along the track 338 GT2R across the MUIS southern subglacial lake (c). The grey regions in (a) and (b) are the subglacial lake boundary from 2018 Sentinel-1a/b DInSAR grounding line product (Mohajerani et al., 2021). In (c), the data are overlaid on the Landsat Image Mosaic of

Antarctica (Bindschadler et al., 2008). The ICESat-2 data used in detecting subglacial lake is version 5 between 30 March 2019 and 22 December 2021.

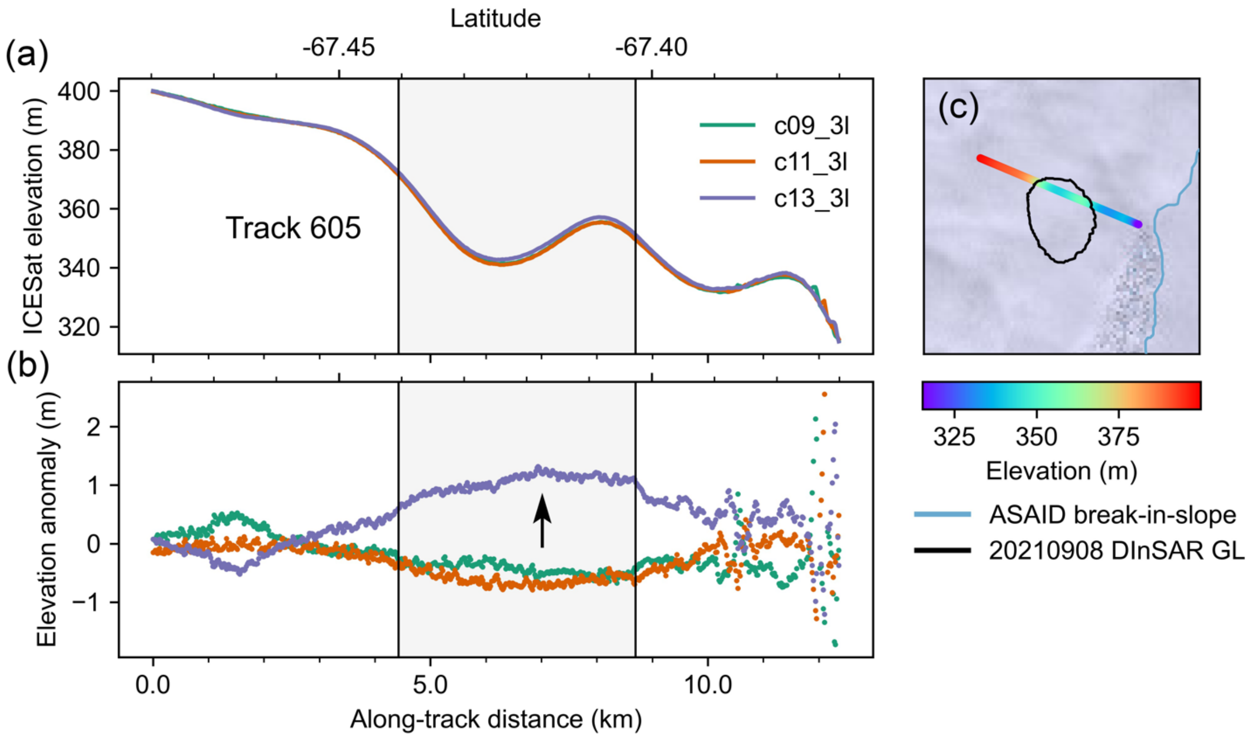


Figure S7. The ICESat-2-derived elevations (a) and elevation anomalies (b) along the track 605 GT3L across the MUIS northern subglacial lake (c). The grey regions in (a) and (b) are the subglacial lake boundary from Sentinel-1a/b DInSAR grounding line on 8 September 2021 mapped in this study (Figure 2g). In (c), the data are overlaid on the Landsat Image Mosaic of Antarctica (Bindschadler et al., 2008). The ICESat-2 data used in detecting subglacial lake is version 5 between 30 March 2019 and 22 December 2021.

Table S1. The grounding line migration between ICESat-2-derived Point F and MEaSUREs 1996 DInSAR grounding line (GL) along the ice flowlines shown in Figure S3a on the Moscow University Ice Shelf. The tidal ranges are derived from the ICESat-2 elevation anomaly profiles.

| Moscow University Ice Shelf | | | | | |
|---|---|---|---|---|---|
| Track number | GL retreat 1996 - 2020 (km) | GL retreat rate 1996 - 2020 (km yr$^{-1}$) | Tidal range (m) | Ice velocity at Point F (m yr$^{-1}$) | Repeat cycles |
| Western flank | | | | | |
| 841-1-l | 13.79 ± 0.1 | 0.57 | 0.89 | 337.5 | 5, 7 |
| 841-1-r | 13.91 ± 0.1 | 0.58 | 0.94 | 337.5 | 5, 7 |
| Eastern flank | | | | | |
| 1108-2-l | 10.95 ± 0.1 | 0.46 | 0.55 | 336.2 | 6, 7 |
| 1108-2-r | 11.13 ± 0.1 | 0.46 | 0.54 | 336.2 | 6, 7 |
| 1283-1-r | 8.71 ± 0.1 | 0.36 | 0.65 | 330.2 | 4, 5 |
| 1108-3-pair | 8.70 ± 0.1 | 0.36 | 0.23 | 329.6 | 6, 7 |
| 1108-3-r | 8.62 ± 0.1 | 0.36 | 0.49 | 329.6 | 6, 7 |
| 1108-3-l | 8.89 ± 0.1 | 0.37 | 0.27 | 330.2 | 6, 7 |
| 1283-1-pair | 9.03 ± 0.1 | 0.38 | 0.61 | 335.1 | 4, 5 |
| 1283-1-l | 8.93 ± 0.1 | 0.37 | 0.61 | 335.1 | 4, 5 |

Table S2. The grounding line migration distance between ICESat-2-derived Point F and MEaSUREs 1996 DInSAR-derived GL along the ice flowlines shown in Figure S3b at the main glacier trunk of the Totten Glacier Ice Shelf. The tidal ranges are derived from the ICESat-2 elevation anomalies at Point H. The time stamp of ICESat-2-derived Point F is defined as year 2020.

| Totten Glacier Ice Shelf | | | | | | | |
|---|---|---|---|---|---|---|---|
| Track number | GL retreat 1996 - 2013 (km) | GL retreat 2013 - 2020 (km) | GL retreat rate 2013 - 2020 (km yr$^{-1}$) | GL retreat rate 1996 - 2013 (km yr$^{-1}$) | Tidal Range (m) | Ice velocity at Point F (m yr$^{-1}$) | Repeat cycles |
| 1207-3-l | 2.08 ± 0.1 | 1.64 ± 0.1 | 0.23 | 0.12 | 2.85 | 828.8 | 4, 5, 8 |
| 1032-1-r | 1.97 ± 0.1 | 2.08 ± 0.1 | 0.30 | 0.12 | 4.89 | 820.7 | 4, 8, 9 |
| 1032-1-l | 1.93 ± 0.1 | 2.33 ± 0.1 | 0.33 | 0.11 | 4.86 | 811.7 | 4, 8, 9 |
| 1032-1-pair | 1.93 ± 0.1 | 2.27 ± 0.1 | 0.32 | 0.11 | 4.91 | 811.7 | 4, 8, 9 |
| 1207-2-r | 2.17 ± 0.1 | 1.45 ± 0.1 | 0.21 | 0.13 | 1.98 | 805.2 | 4, 5, 8 |
| 1207-2-pair | 2.16 ± 0.1 | 1.41 ± 0.1 | 0.20 | 0.13 | 2.11 | 805.2 | 4, 5, 8 |
| 1032-2-l | 2.04 ± 0.1 | 1.37 ± 0.1 | 0.20 | 0.12 | 3.86 | 753.9 | 3,4,8,9,10 |
| 1032-2-pair | 2.03 ± 0.1 | 1.38 ± 0.1 | 0.20 | 0.12 | 3.96 | 753.9 | 3,4,8,9,10 |
| 1032-2-r | 2.02 ± 0.1 | 1.40 ± 0.1 | 0.20 | 0.12 | 3.92 | 753.9 | 3,4,8,9,10 |
| 1207-1-r | 2.03 ± 0.1 | 0.81 ± 0.1 | 0.12 | 0.12 | 0.83 | 715.8 | 4, 5 |
| 1207-1-l | 2.05 ± 0.1 | 0.77 ± 0.1 | 0.11 | 0.12 | 1.06 | 715.8 | 4, 5 |
| 1207-1-pair | 2.04 ± 0.1 | 0.75 ± 0.1 | 0.11 | 0.12 | 1.09 | 715.8 | 4, 5 |

Table S3. The acquisition time of ERS-1/2 SAR images used in 1996 MEaSUREs DInSAR grounding line mapping. The tidal amplitudes are calculated at location -66.3102°S, 122.6998°E on Moscow University Ice Shelf (MUIS) and -66.9212°S, 117.2723°E on the Totten Glacier Ice Shelf eastern channel (TGIS East Channel) from CATS2008 (Padman et al., 2002) and FES2014 tidal models (Lyard et al., 2021). The absolute tidal range at four satellite passes used in DInSAR interferogram mapping is calculated as |h1+h4-h2-h3| where h1, h2, h3, h4 are the modelled tidal amplitude at each time stamp (Fricker et al., 2009).

| Time of SAR pass | Latitude | Longitude | CATS2008 tide amplitude (cm) | FES2014 tide amplitude (cm) | CATS2008 absolute tide range (cm) | FES2014 absolute tide range (cm) |
|---|---|---|---|---|---|---|
| MUIS | | | | | | |
| 19960214T003648 | -66.3102 | 122.6998 | -34.51 | -38.25 | 11.22 | 10.76 |
| 19960215T003651 | -66.3102 | 122.6998 | -31.01 | -35.28 | | |
| 19960320T003651 | -66.3102 | 122.6998 | -18.79 | -21.90 | | |
| 19960321T003650 | -66.3102 | 122.6998 | -26.51 | -29.69 | | |
| TGIS | | | | | | |
| 19960310T005108 | -66.9212 | 117.2723 | -44.66 | -47.27 | 8.60 | 9.77 |
| 19960311T005107 | -66.9212 | 117.2723 | -45.44 | -47.68 | | |
| 19960414T005110 | -66.9212 | 117.2723 | 3.71 | 2.00 | | |
| 19960415T005109 | -66.9212 | 117.2723 | 11.53 | 11.36 | | |

Table S4. Modelled tidal amplitudes and grounding line (GL) retreat compared with 1996 MEaSUREs GL for Sentinel-1a/b interferograms at the Moscow University Ice Shelf (MUIS) main glacier trunk. t1, t2 and t3 are the time stamps for each SAR pass. h1, h2 and h3 are the tidal amplitude predictions at each acquisition date calculated from CATS2008 (Padman et al., 2002) and FES2014 tidal models (Lyard et al., 2021). The tidal amplitudes are used to identify $h_{max}$, the highest positive tides among all different tides ($h_{max}$=max($h_1$, $h_2$, $h_3$)) (Brancato et al., 2020). The differential tidal predictions $|\delta h|$ from the tidal models for each Sentinel-1a/b DInSAR interferogram are calculated as $|\delta h| = |(h3 - h2) - (h2 - h1)|$.

| Time stamp of SAR pass 1 (t1) | Time stamp of SAR pass 2 (t2) | Time stamp of SAR pass 3 (t3) | Modelled tide amplitude h1 at t1 (cm) | Modelled tide amplitude h2 at t2 (cm) | Modelled tide amplitude h3 at t3 (cm) | $h_{max}$ (cm) | $|\delta h|$ (cm) | GL retreat since 1996 along ice flowline in Figure 2 (km) |
|---|---|---|---|---|---|---|---|---|
| CATS2008 Tide Model (-67.0714°S, 120.6249°E) | | | | | | | | |
| 20210417T121114 | 20210423T121156 | 20210429T121114 | -27.95 | 34.80 | -80.60 | 34.80 | 178.15 | 3.14 ± 0.13 |
| 20210423T121156 | 20210429T121114 | 20210505T121156 | 34.80 | -80.60 | 32.45 | 34.80 | 228.45 | 5.67 ± 0.13 |
| 20210429T121114 | 20210505T121156 | 20210511T121115 | -80.60 | 32.45 | -50.80 | 32.45 | 196.30 | 3.84 ± 0.13 |
| FES2014 Tide Model (-66.3102°S, 122.6998°E) | | | | | | | | |
| 20210417T121114 | 20210423T121156 | 20210429T121114 | -28.71 | 35.42 | -75.53 | 35.42 | 175.08 | 3.14 ± 0.13 |
| 20210423T121156 | 20210429T121114 | 20210505T121156 | 35.42 | -75.53 | 33.79 | 35.42 | 220.28 | 5.67 ± 0.13 |
| 20210429T121114 | 20210505T121156 | 20210511T121115 | -75.53 | 33.79 | -44.66 | 33.79 | 187.78 | 3.84 ± 0.13 |

Table S5. Modelled tidal amplitudes and grounding line (GL) retreat compared with 1996 MEaSUREs GL for Sentinel-1a/b interferograms at the Totten East branch ice stream (Fig. 6). t1, t2 and t3 are the time stamps for each SAR pass. h1, h2 and h3 are the tidal amplitude predictions at each acquisition date calculated from CATS2008 (Padman et al., 2002) and FES2014 tidal models (Lyard et al., 2021). The tidal amplitudes are used to identify $h_{max}$, the highest positive tides among all different tides ($h_{max}=max(h_1, h_2, h_3)$) (Brancato et al., 2020). The differential tidal predictions $|\delta h|$ from the tidal models for each Sentinel-1a/b DInSAR interferogram are calculated as $|\delta h| = |(h3 - h2) - (h2 - h1)|$.

| Time stamp of SAR pass 1 (t1) | Time stamp of SAR pass 2 (t2) | Time stamp of SAR pass 3 (t3) | Modelled tide amplitude h1 at t1 (cm) | Modelled tide amplitude h2 at t2 (cm) | Modelled tide amplitude h3 at t3 (cm) | $h_{max}$ (cm) | $\lvert\delta h\rvert$(cm) | GL retreat since 1996 along ice flowline in Figure 6 (km) |
|---|---|---|---|---|---|---|---|---|
| CATS2008 Tidal Model (-67.0043°S, 115.8222°E) | | | | | | | | |
| 20180301T123555 | 20180307T123513 | 20180313T123556 | -2.64 | -23.07 | 34.82 | 34.82 | 78.31 | 5.15 ± 0.13 |
| 20190119T123603 | 20190125T123521 | 20190131T123602 | 62.07 | -51.09 | 50.53 | 62.07 | 214.77 | 4.84 ± 0.13 |
| 20190302T123520 | 20190308T123602 | 20190314T123520 | 40.04 | -47.65 | 12.88 | 40.04 | 148.21 | 6.57 ± 0.13 |
| 20190308T123602 | 20190314T123520 | 20190320T123602 | -47.65 | 12.88 | -14.5 | 12.88 | 87.9 | 6.45 ± 0.13 |
| 20190507T123603 | 20190513T123522 | 20190519T123604 | -67.43 | 31.79 | -67.92 | 31.79 | 198.93 | 6.96 ± 0.13 |
| 20200308T123526 | 20200314T123608 | 20200320T123527 | 21.77 | -36.85 | 32.65 | 32.65 | 128.13 | 4.64 ± 0.13 |
| 20200401T123527 | 20200407T123609 | 20200413T123527 | 15.07 | -28.61 | -9.58 | 15.07 | 62.71 | 6.76 ± 0.13 |
| 20200718T123532 | 20200724T123615 | 20200730T123533 | -40 | -47 | -29.78 | -29.78 | 24.23 | 6.06 ± 0.13 |
| 20210309T123614 | 20210315T123532 | 20210321T123614 | 54.46 | -57.46 | 11.93 | 54.46 | 181.31 | 6.4 ± 0.13 |
| 20210402T123614 | 20210408T123533 | 20210414T123615 | -35.04 | 22.07 | -62.81 | 22.07 | 141.99 | 5.58 ± 0.13 |
| 20210420T123533 | 20210426T123615 | 20210502T123534 | 17.55 | -42.46 | -3.08 | 17.55 | 99.37 | 6 ± 0.13 |
| FES2014 Tidal Model (-66.6687°S, 116.4448°E) | | | | | | | | |
| 20180301T123555 | 20180307T123513 | 20180313T123556 | 3.42 | -20.85 | 38.46 | 38.46 | 83.58 | 5.15 ± 0.13 |
| 20190119T123603 | 20190125T123521 | 20190131T123602 | 66.61 | -48.72 | 55.54 | 66.61 | 219.59 | 4.84 ± 0.13 |
| 20190302T123520 | 20190308T123602 | 20190314T123520 | 43.98 | -43.14 | 15.77 | 43.98 | 146.04 | 6.57 ± 0.13 |
| 20190308T123602 | 20190314T123520 | 20190320T123602 | -43.14 | 15.77 | -7.77 | 15.77 | 82.46 | 6.45 ± 0.13 |
| 20190507T123603 | 20190513T123522 | 20190519T123604 | -65.6 | 32.93 | -66.61 | 32.93 | 198.06 | 6.96 ± 0.13 |
| 20200308T123526 | 20200314T123608 | 20200320T123527 | 28.23 | -34.34 | 36.6 | 36.6 | 133.52 | 4.64 ± 0.13 |
| 20200401T123527 | 20200407T123609 | 20200413T123527 | 17.94 | -23.34 | -7.06 | 17.94 | 57.57 | 6.76 ± 0.13 |
| 20200718T123532 | 20200724T123615 | 20200730T123533 | -42.74 | -47.63 | -31.76 | -31.76 | 20.77 | 6.06 ± 0.13 |
| 20210309T123614 | 20210315T123532 | 20210321T123614 | 60.17 | -52.41 | 13.72 | 60.17 | 178.71 | 6.4 ± 0.13 |
| 20210402T123614 | 20210408T123533 | 20210414T123615 | -32.04 | 27.58 | -58.51 | 27.58 | 145.71 | 5.58 ± 0.13 |
| 20210420T123533 | 20210426T123615 | 20210502T123534 | 21.23 | -38.59 | -0.27 | 21.23 | 98.14 | 6 ± 0.13 |

Table S6. Modelled tidal amplitudes and grounding line (GL) retreat compared with 1996 MEaSUREs GL for Sentinel-1a/b interferograms at the Moscow University western ice shelf channel (Fig. 9). t1, t2 and t3 are the time stamps for each SAR pass. h1, h2 and h3 are the tidal amplitude predictions at each acquisition date calculated from CATS2008 (Padman et al., 2002) and FES2014 tidal models (Lyard et al., 2021). The tidal amplitudes are used to identify $h_{max}$, the highest positive tides among all different tides ($h_{max}=max(h_1, h_2, h_3)$) (Brancato et al., 2020). The differential tidal predictions $|\delta h|$ from the tidal models for each Sentinel-1a/b DInSAR interferogram are calculated as $|\delta h| = |(h3 - h2) - (h2 - h1)|$.

| Time stamp of SAR pass 1 (t1) | Time stamp of SAR pass 2 (t2) | Time stamp of SAR pass 3 (t3) | Modelled tide amplitude h1 at t1 (cm) | Modelled tide amplitude h2 at t2 (cm) | Modelled tide amplitude h3 at t3 (cm) | $h_{max}$ (cm) | $\lvert\delta h\rvert$(cm) | Channel width (m) |
|---|---|---|---|---|---|---|---|---|
| CATS2008 Tidal Model (-67.1023°S, 117.7366°E) | | | | | | | | |
| 20180304T121054 | 20180310T121136 | 20180316T121054 | -62.14 | 29.49 | -11.27 | 29.49 | 132.39 | 3128 ± 127 |
| 20180322T121136 | 20180328T121054 | 20180403T121136 | -35.22 | 34.07 | -58.69 | 34.07 | 162.05 | 1442 ± 127 |
| 20200305T121107 | 20200311T121149 | 20200317T121107 | 56.86 | -73.25 | 43.57 | 56.86 | 246.94 | 2666 ± 127 |
| 20210411T121155 | 20210417T121114 | 20210423T121156 | -39.42 | -24.30 | 32.23 | 32.23 | 41.41 | 0 |

| | | | | | | | | |
|---|---|---|---|---|---|---|---|---|
| 20210417T121114 | 20210423T121156 | 20210429T121114 | -24.30 | 32.23 | -78.33 | 32.23 | 167.09 | 2187 ± 127 |
| 20210423T121156 | 20210429T121114 | 20210505T121156 | 32.23 | -78.33 | 32.30 | 32.30 | 221.19 | 2837 ± 127 |
| 20210429T121114 | 20210505T121156 | 20210511T121115 | -78.33 | 32.30 | -52.78 | 32.30 | 195.71 | 1621 ± 127 |
| FES2014 Tidal Model (-66.9736°S, 117.8411°E) | | | | | | | | |
| 20180304T121054 | 20180310T121136 | 20180316T121054 | -61.70 | 30.80 | -9.28 | 30.80 | 132.57 | 3128 ± 127 |
| 20180322T121136 | 20180328T121054 | 20180403T121136 | -33.21 | 38.45 | -57.74 | 38.45 | 167.85 | 1442 ± 127 |
| 20200305T121107 | 20200311T121149 | 20200317T121107 | 59.16 | -71.76 | 48.36 | 59.16 | 251.06 | 2666 ± 127 |
| 20210411T121155 | 20210417T121114 | 20210423T121156 | -37.07 | -25.06 | 34.98 | 34.98 | 48.02 | 0 |
| 20210417T121114 | 20210423T121156 | 20210429T121114 | -25.06 | 34.98 | -77.36 | 34.98 | 172.37 | 2187 ± 127 |
| 20210423T121156 | 20210429T121114 | 20210505T121156 | 34.98 | -77.36 | 37.37 | 37.37 | 227.07 | 2837 ± 127 |
| 20210429T121114 | 20210505T121156 | 20210511T121115 | -77.36 | 37.37 | -50.22 | 37.37 | 202.32 | 1621 ± 127 |

Table S7. Modelled tidal amplitudes and grounding line (GL) retreat compared with 1996 MEaSUREs GL for Sentinel-1a/b interferograms at the Totten eastern ice shelf channel (Fig. 8). t1, t2 and t3 are the time stamps for each SAR pass. h1, h2 and h3 are the tidal amplitude predictions at each acquisition date calculated from CATS2008 (Padman et al., 2002) and FES2014 tidal models (Lyard et al., 2021). The tidal amplitudes are used to identify $h_{max}$, the highest positive tides among all different tides ($h_{max}=max(h_1, h_2, h_3)$) (Brancato et al., 2020). The differential tidal predictions $|\delta h|$ from the tidal models for each Sentinel-1a/b DInSAR interferogram are calculated as $|\delta h| = |(h3 - h2) - (h2 - h1)|$.

| Time stamp of SAR pass 1 (t1) | Time stamp of SAR pass 2 (t2) | Time stamp of SAR pass 3 (t3) | Modelled tide amplitude h1 at t1 (cm) | Modelled tide amplitude h2 at t2 (cm) | Modelled tide amplitude h3 at t3 (cm) | $h_{max}$ (cm) | $\|\delta h\|$ (cm) | Channel width (m) |
|---|---|---|---|---|---|---|---|---|
| CATS2008 Tidal Model (-67.0131°S, 117.0389°E) | | | | | | | | |
| 20170818T121137 | 20170824T121056 | 20170830T121138 | -30.65 | -49.05 | -24.28 | -24.28 | 43.16 | 0 |
| 20171101T123559 | 20171107T123517 | 20171113T123558 | 12.19 | -36.40 | 10.85 | 12.19 | 95.83 | 2950 ± 127 |
| 20180304T121054 | 20180310T121136 | 20180316T121054 | -62.85 | 29.88 | -12.60 | 29.88 | 135.20 | 3858 ± 127 |
| 20180310T121136 | 20180316T121054 | 20180322T121136 | 29.88 | -12.60 | -34.79 | 29.88 | 20.29 | 0 |
| 20180322T121136 | 20180328T121054 | 20180403T121136 | -34.79 | 33.19 | -59.05 | 33.19 | 160.22 | 1814 ± 127 |
| 20190305T121142 | 20190311T121101 | 20190317T121142 | -5.50 | -39.57 | 58.67 | 58.67 | 132.31 | 1749 ± 127 |
| 20190311T121101 | 20190317T121142 | 20190323T121101 | -39.57 | 58.67 | -73.56 | 58.67 | 230.47 | 3505 ± 127 |
| 20190317T121142 | 20190323T121101 | 20190329T121143 | 58.67 | -73.56 | 34.32 | 58.67 | 240.10 | 3893 ± 127 |
| 20200715T121113 | 20200721T121155 | 20200727T121113 | -16.48 | -59.61 | -16.65 | -16.48 | 86.09 | 0 |
| 20200727T121113 | 20200802T121156 | 20200808T121114 | -16.65 | -51.45 | -31.80 | -16.65 | 54.45 | 1236 ± 127 |
| 20200814T121156 | 20200820T121115 | 20200826T121157 | -30.25 | -56.06 | -32.94 | -30.25 | 48.92 | 1516 ± 127 |
| 20210411T121155 | 20210417T121114 | 20210423T121156 | -40.75 | -24.00 | 31.79 | 31.79 | 39.04 | 0 |
| 20210417T121114 | 20210423T121156 | 20210429T121114 | -24.00 | 31.79 | -78.84 | 31.79 | 166.41 | 2613 ± 127 |
| 20210423T121156 | 20210429T121114 | 20210505T121156 | 31.79 | -78.84 | 32.39 | 32.39 | 221.86 | 2887 ± 127 |
| FES2014 Tidal Model (-66.9212°S, 117.2723°E) | | | | | | | | |
| 20170818T121137 | 20170824T121056 | 20170830T121138 | -34.18 | -51.70 | -27.03 | -27.03 | 42.19 | 0 |
| 20171101T123559 | 20171107T123517 | 20171113T123558 | 10.35 | -35.61 | 12.57 | 12.57 | 94.14 | 2950 ± 127 |
| 20180304T121054 | 20180310T121136 | 20180316T121054 | -61.90 | 31.06 | -9.95 | 31.06 | 133.97 | 3858 ± 127 |
| 20180310T121136 | 20180316T121054 | 20180322T121136 | 31.06 | -9.95 | -32.80 | 31.06 | 18.16 | 0 |
| 20180322T121136 | 20180328T121054 | 20180403T121136 | -32.80 | 38.00 | -57.80 | 38.00 | 166.60 | 1814 ± 127 |
| 20190305T121142 | 20190311T121101 | 20190317T121142 | -2.51 | -39.54 | 62.50 | 62.50 | 139.07 | 1749 ± 127 |
| 20190311T121101 | 20190317T121142 | 20190323T121101 | -39.54 | 62.50 | -72.47 | 62.50 | 237.01 | 3505 ± 127 |
| 20190317T121142 | 20190323T121101 | 20190329T121143 | 62.50 | -72.47 | 36.94 | 62.50 | 244.38 | 3893 ± 127 |
| 20200715T121113 | 20200721T121155 | 20200727T121113 | -16.49 | -59.69 | -17.72 | -16.49 | 85.17 | 0 |
| 20200727T121113 | 20200802T121156 | 20200808T121114 | -17.72 | -53.95 | -33.99 | -17.72 | 56.20 | 1236 ± 127 |
| 20200814T121156 | 20200820T121115 | 20200826T121157 | -33.30 | -56.60 | -34.18 | -33.30 | 45.73 | 1516 ± 127 |
| 20210411T121155 | 20210417T121114 | 20210423T121156 | -37.74 | -24.78 | 34.70 | 34.70 | 46.51 | 0 |
| 20210417T121114 | 20210423T121156 | 20210429T121114 | -24.78 | 34.70 | -77.50 | 34.70 | 171.67 | 2613 ± 127 |
| 20210423T121156 | 20210429T121114 | 20210505T121156 | 34.70 | -77.50 | 37.39 | 37.39 | 227.08 | 2887 ± 127 |

## References


Bindschadler, R., Vornberger, P., Fleming, A., Fox, A., Mullins, J., Binnie, D., Paulsen, S. J., Granneman, B. and Gorodetzky, D.: The Landsat Image Mosaic of Antarctica, Remote Sens. Environ., 112(12), 4214–4226, doi:10.1016/J.RSE.2008.07.006, 2008.

Brancato, V., Rignot, E., Milillo, P., Morlighem, M., Mouginot, J., An, L., Scheuchl, B., Jeong, S., Rizzoli, P., Bueso Bello, J. L. and Prats-Iraola, P.: Grounding Line Retreat of Denman Glacier, East Antarctica, Measured With COSMO-SkyMed Radar Interferometry Data, Geophys. Res. Lett., 47(7), doi:10.1029/2019GL086291, 2020.

ESA: Antarctic Ice Sheet Climate Change Initiative, Grounding Line Locations for the Denman and Totten Glaciers, Antarctica, 2011–2017, v1.0, Cent. Environ. Data Anal., 2017.

Fricker, H. A., Coleman, R., Padman, L., Scambos, T. A., Bohlander, J. and Brunt, K. M.: Mapping the grounding zone of the Amery Ice Shelf, East Antarctica using InSAR, MODIS and ICESat, Antarct. Sci., doi:10.1017/S095410200999023X, 2009.

Lyard, F. H., Allain, D. J., Cancet, M., Carrère, L. and Picot, N.: FES2014 global ocean tide atlas: Design and performance, Ocean Sci., 17(3), 615–649, doi:10.5194/OS-17-615-2021, 2021.

Mohajerani, Y., Jeong, S., Scheuchl, B., Velicogna, I., Rignot, E. and Milillo, P.: Automatic delineation of glacier grounding lines in differential interferometric synthetic-aperture radar data using deep learning, Sci. Rep., 11(1), 4992, doi:10.1038/s41598-021-84309-3, 2021.

Morlighem, M., Rignot, E., Binder, T., Blankenship, D., Drews, R., Eagles, G., Eisen, O., Ferraccioli, F., Forsberg, R., Fretwell, P., Goel, V., Greenbaum, J. S., Gudmundsson, H., Guo, J., Helm, V., Hofstede, C., Howat, I., Humbert, A., Jokat, W., Karlsson, N. B., Lee, W. S., Matsuoka, K., Millan, R., Mouginot, J., Paden, J., Pattyn, F., Roberts, J., Rosier, S., Ruppel, A., Seroussi, H., Smith, E. C., Steinhage, D., Sun, B., Broeke, M. R. va. den, Ommen, T. D. va., Wessem, M. van and Young, D. A.: Deep glacial troughs and stabilizing ridges unveiled beneath the margins of the Antarctic ice sheet, Nat. Geosci., 13(2), 132–137, doi:10.1038/s41561-019-0510-8, 2020.

Padman, L., Fricker, H. A., Coleman, R., Howard, S. and Erofeeva, L.: A new tide model for the Antarctic ice shelves and seas, Ann. Glaciol., 34, 247–254, doi:10.3189/172756402781817752, 2002.

Rignot, E., Mouginot, J. and Scheuchl, B.: Antarctic grounding line mapping from differential satellite radar interferometry, Geophys. Res. Lett., doi:10.1029/2011GL047109, 2011.

Rignot, E., Mouginot, J. and Scheuchl, B.: MEaSUREs Antarctic Grounding Line from Differential Satellite Radar Interferometry, Version 2. Boulder, Colorado USA, , doi:https://doi.org/10.5067/IKBWW4RYHF1Q, 2016.